Applied Surface Science 612 (2023) 155782

Contents lists available at ScienceDirect

Applied Surface Science

journal homepage: www.elsevier.com/locate/apsusc

Full Length Article

Confinement effects of carbonized polymer dots and directional migration of $ZnIn_2S_4$ photogenerated charge carriers for enhanced water purification

Xingwang Yan [a], Xiaolin Zhang [b], Bin Wang [a,b], Ziran Chen [c], Junze Zhao [a], Gaopeng Liu [a], Dan Li [b], Qingdong Ruan [b], Liangliang Liu [b], Yue Xu [b], Mengxia Ji [a], Paul K. Chu [b], Huaming Li [a], Jiexiang Xia [a,*]

[a] School of Chemistry and Chemical Engineering, Institute for Energy Research, Jiangsu University, 301 Xuefu Road, Zhenjiang 212013, China
[b] Department of Physics, Department of Materials Science and Engineering, and Department of Biomedical Engineering, City University of Hong Kong, Tat Chee Avenue, Kowloon, Hong Kong, China
[c] Department of Architecture and Environment Engineering, Sichuan Vocational and Technical College, Suining 629000, Sichuan, China

ARTICLE INFO

Keywords:
$ZnIn_2S_4$
CPDs
Z-scheme heterojunction
Photocatalysis
Confinement effects

ABSTRACT

Efficient heterojunction photocatalysts with spatial separation of photogenerated carriers are crucial to photocatalysis. Herein, the unique carbonized polymer dots/$ZnIn_2S_4$ (CPDs/ZIS) Z-scheme heterojunction is designed to realize efficient spatial directional separation of photogenerated carriers. The CPDs broaden the light absorption range of ZIS and lengthen the lifetime of photogenerated charges. As the enrichment center of photogenerated electrons and active site of activated oxygen, CPDs generate more superoxide radicals to facilitate mineralization of organic pollutants by means of confined catalysis. The Z-scheme migration mechanism of photogenerated carriers in the CPDs/ZIS composite preserves the original valence band potential of ZIS and retains more holes for oxidation. Compared to the pristine ZIS, the CPDs/ZIS composite delivers enhanced photocatalytic performance in pollutant degradation. Electron spin resonance spectroscopy, free radical capture experiments, and liquid chromatography/mass spectrometry are performed to elucidate the photocatalytic mechanism of CPDs/ZIS.

1. Introduction

Energy shortage and environmental pollution are becoming increasingly serious in the modern society [1,2] and environmentally friendly and economical semiconductor photocatalysis utilizing sunlight is one of the preferred solutions [3–5]. Although carbon nitride [6,7], metal oxides [8], sulfides [9,10] and bismuth-based oxyhalides [11,12] have been proposed as photocatalysts for this purpose, the photocatalytic conversion efficiency still cannot meet commercial demand due to the low solar energy utilization rates, weak redox potentials and recombination of photo-generated electron-hole pairs [13–16]. Therefore, new and more efficient materials must be developed [17,18].

In photocatalytic systems, heterojunctions are commonly employed to improve the separation efficiency of photogenerated carriers [19–21]. In particular, Z-scheme heterojunctions not only accelerate spatial separation of photoinduced charges, but also retain the high redox capability of the materials [22,23]. Z-scheme heterojunctions are constructed by putting two semiconductors with the appropriate energy band structure in close contact to produce an internal electric field. Upon light irradiation, photogenerated electrons migrate from the conduction band (CB) of the low energy band structure to the valence band (VB) of the high energy band structure and recombine with holes under the internal electric field. Electrons with the strong reduction ability and holes with the strong oxidation ability are retained in the conduction and valence bands of two materials, respectively.

In recent years, transition metal sulfides have aroused interests because of the unique optical and electronic characteristics [24,25]. For example, ZIS shows good photocatalytic properties because of the large specific area, adjustable bandgap, and excellent light absorption [26–28]. However, in single ZIS photocatalysts, spontaneous aggregation of ZIS nanosheets decreases the active sites and causes serious recombination of photo-excited charges consequently reducing the photocatalytic efficiency [29]. ZIS forms heterojunctions with other semiconductors such as MoO_3 [30], ZnS [31], and $BiVO_4$ [32], which

* Corresponding author.
E-mail address: xjx@ujs.edu.cn (J. Xia).

https://doi.org/10.1016/j.apsusc.2022.155782
Received 12 September 2022; Received in revised form 8 November 2022; Accepted 17 November 2022
Available online 21 November 2022
0169-4332/© 2022 Elsevier B.V. All rights reserved.

can enhance charge transfer at the interface. Wang et al., have shown that the Z-scheme Sv-$ZnIn_2S_4/MoSe_2$ photocatalyst modulated by an internal electric field exhibits good hydrogen evolution [33]. As zero-dimension carbon-based nanomaterials, CPDs are widely used in applications such as light conversion, biological imaging, and luminescence devices due to the abundant sources, low cost, excellent photoelectric properties, and good stability [34–37]. In addition, CPDs are excellent electron transporters and acceptors as a result of the conjugated π structure [38] rendering them useful in photocatalysis. Introducing a small amount of CPDs as local active sites into other photocatalytic materials can improve light trapping capability, separate photogenerated electrons and holes, and improve the photocatalytic conversion efficiency. According to the characteristics of ZIS and CPDs, the Z-scheme heterojunction comprising CPDs and ZIS is expected to have good photocatalytic properties.

Herein, the flower-like Z-scheme CPDs/ZIS composite with matching band structures are designed and fabricated. Electron transfer in the CPDs/ZIS system is analyzed by X-ray photoelectron spectroscopy (XPS) and electron spin-resonance spectroscopy (ESR) revealing the direct Z-scheme mechanism. Introduction of CPDs enhances the light capturing capability and more photons participate in the photocatalytic reaction. More importantly, CPDs become electron enriched and generate more reactive oxygen species $\cdot O_2^-$ due to the confinement effects of CPDs and enhanced degradation of rhodamine B (RhB) and 2-mercaptobenzothiazole (MBT) is ascommplished. The mineralization rates of CPDs/ZIS for RhB and MBT are 2.1 times and 2.3 times larger than those of pure ZIS. The results provide insights into the design and preparation of efficient photocatalysts materials for degradation of pollutants.

2. Experimental section

2.1. Chemicals and reagents

Zinc chloride ($ZnCl_2$) and indium chloride tetrahydrate ($InCl_3{\cdot}4H_2O$) were purchased from Shanghai Aladdin Biochemical Technology Co., Ltd. Thioacetamide (TAA), glycerol, citric acid monohydrate and ethylenediamine were received from Sinopharm Chemical Reagent Co., Ltd. All the reagents were used without purification and distilled water was used to prepare the solutions.

2.2. Materials synthesis

Synthesis of CPDs: 5 mmol citric acid was dissolved in 10 ml of distilled water and 335 μL of ethylenediamine were added and stirred for 30 min. The solution was placed in a 25 ml Teflon-lined autoclave and heated to 200 °C for 5 h. After cooling to room temperature, the solution was poured into a dialysis bag and dialyzed for 24 h to remove macromolecular impurities. The dialyzed solution was freeze-dried for 72 h and the brown solid obtained was CPDs.

Synthesis of flower-like ZIS: 4 mmol $ZnCl_2$, 10 ml of HCl (pH = 2.5), and 3 ml of glycerol were sonicated in a 50 ml round bottom flask to form solution A. 4 mmol $InCl_3{\cdot}4H_2O$ and 8 mmol TAA were added to 10 ml of HCl (pH = 2.5) to form solutions B and solution C, respectively. Solutions B and C were added slowly to solution A and stirred for half an hour. It was then transferred to oil bath and the reaction proceeded at 80 °C for 2 h. The product was washed three times with distilled water and ethanol and dried in the vacuum oven at 45 °C for 6 h. The sample was ZIS.

Synthesis of CPDs/ZIS composites: Synthesis of the CPDs/ZIS composites is illustrated in Fig. 1. 4 mmol $ZnCl_2$, 10 ml of HCl (pH = 2.5), and 3 ml of glycerol were sonicated in a 50 ml round bottom flask to form solution A. 4 mmol $InCl_3{\cdot}4H_2O$ and 8 mmol TAA were dissolved in 10 ml of HCl (pH = 2.5) to form solutions B and solution C, respectively. Solutions B and C were added slowly to solution A and stirred. 8.5 mg, 26.2 mg, 44.5 mg, 63.7 mg and 104.6 mg of CPDs were added to the solution, respectively and the following steps are the same as those for ZIS. The samples were designated as 1 wt% CPDs/ZIS, 3 wt% CPDs/ZIS, 5 wt% CPDs/ZIS, 7 wt% CPDs/ZIS and 11 wt% CPDs/ZIS, respectively.

2.3. Characterization

Scanning electron microscopy (SEM, JOEL JSM-7800F), transmission electron microscopy (TEM, Fei talos 200x), and high-resolution transmission electron microscopy (HR-TEM, Fei talos 200x) were used to examine the morphology of the catalysts. X-ray diffraction (XRD) was performed on the Shimadzu XRD-6000X-ray diffractometer with Cu K_α irradiation. Raman scattering spectra were obtained on the Raman spectroscope (DXR, Thermo Fisher) and Fourier transform infrared (FTIR) spectra was acquired on the Nicolet iS50 (Thermo Electron Corporation). XPS (Thermo ESCALAB 250Xi) was carried out to analyze the elemental composition and chemical states of the samples. UV–vis diffuse reflectance spectra (UV–vis DRS) were obtained on the UV-3600 Plus spectrophotometer (Shimadzu Corporation, Japan). The intermediates formed during TC degradation were monitored by LC-MS (Thermo, *thermo LXQ LC/MS) in which the mobile phase contained 30 % methanol and 70 % water. The specific surface area and particle size were determined based on the N_2 adsorption–desorption isotherms using the surface area analyzer (Micromeritics Instrument Corporation, USA). The electrochemical impedance spectroscopy (EIS) and Mott-Schottky plots were collected from the phosphate buffer solution, 0.1 M KCl and 5 mM $Fe(CN)_6^{3-}/Fe(CN)_6^{4-}$, and 0.1 M KCl solution. The electrochemical signals were recorded on the CHI 760E electrochemical analyzer (Chenhua Instrument Company).

All the density functional theory (DFT) calculations were carried out by the *Vienna ab initio simulation package* (VASP) with the projector augmented wave (PAW) method. The gradient approximation (GGA) with Perdew-Burke-Ernzerhof (PBE) functional was applied as the exchange-correlation functional. The CPDs cluster model, the ZIS layer model and CPDs/ZIS model were established with the 15 Å vacuum layer. During the optimization and work function calculations, the cut-off energy was set as 420 eV. The energy and force convergence criteria were set at 1×10^{-4} eV per atom and −0.05 eV $Å^{-1}$, respectively. The K-points of CPDs cluster model was set as $0 \times 0 \times 0 \times 1$ while the K-points of ZIS layer model and CPDs/ZIS model were set as $3 \times 3 \times 1$. Finally, the work function results of models were exported by the

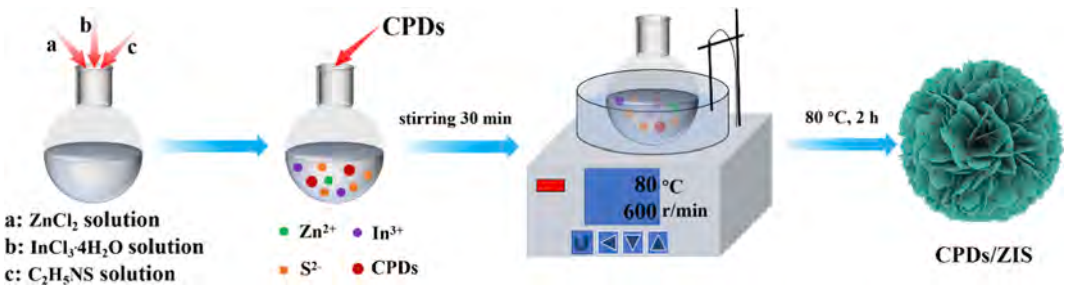

Fig. 1. Schematic illustration of the synthesis of CPDs/ZIS.

script *Vaspkit*.

2.4. Photocatalytic experiments

The samples weighing 10 mg were mixed with 100 ml of the RhB solution (10 mg/L) and 50 mg of the sample were added to 100 ml of the MBT solution (10 mg/L). Circulating water maintained the temperature in the degradation reaction at 30 °C and an air pump provided ample oxygen in the reaction. The Pyrex photocatalytic reactor consisted of a 420 nm cut-off filter and 250 W Xe lamp to emit visible light. Before light irradiation, the suspension was stirred for 0.5 h to achieve adsorption and desorption equilibrium between the photocatalysts and pollutant in darkness. 4 ml of the suspension were collected every 30 min and centrifuged to remove the particles from the suspensions. The absorbance of the RhB and MBT solutions was measured by UV–vis spectrophotometry at 553 nm and 320 nm.

3. Results and discussion

The morphology of ZIS and CPDs/ZIS are examined by SEM and TEM. As shown by the SEM image in Fig. 2**a**, ZIS has a layered petal-like spherical structure. The microsphere is about 2 μm in diameter and consists of a number of ultra-thin nanosheets (Fig. 2**b**). This layered sheet-like structure facilitates light harvesting on account of multiple light scattering between ZIS nanosheets [39]. Furthermore, the nanosheets expose a larger surface area and provide more active sites so that more pollutants can be degraded. The HR-TEM images of ZIS in Fig. 2**c** reveal lattice spacings of 0.32 nm and 0.31 nm corresponding to the (1 0 2) crystal facets of ZIS. After introduction of CPDs, the microstructure of ZIS is almost unchanged (Fig. 2**d, e**) indicating CPDs do not affect the growth of ZIS. Fig. 2**f** depicts the HR-TEM of CPDs/ZIS. In addition to the 0.32 nm lattice spacing assigned to the (1 0 2) crystal surface of ZIS, the lattice fringe of 0.21 nm is attributed to CPDs. Interleaving of the lattice stripes confirms that CPDs are incorporated into ZIS. Fig. 2**g** shows that Zn, In, S, C, N, and O are uniformly distributed in CPDs/ZIS.

The adsorption capacity is assessed according to the nitrogen adsorption and desorption isotherms (**Fig. S1**). The type IV isotherms with H_3 hysteresis loops indicate the presence of mesopores [40,41] consistent with the SEM image of ZIS. Fig. S1**b-f** show that the specific surface area increases initially and then decreases with increasing CPDs concentration. Since a larger adsorption area and more surface active sites are beneficial to photocatalytic performance, improved photocatalytic degradation is expected.

XRD is carried out to determine the crystallographic structure and Fig. 3**a** shows that the XRD pattern of ZIS matches that of the hexagonal phase (JCPDS NO. 65-2023) [42]. The main diffraction peaks at 21.4°, 27.6°, 47.2°, 52.4°, and 55.6° are assigned to the (0 0 6), (1 0 2), (1 1 0), (1 1 6) and (0 2 2) crystal facets of ZIS, respectively. There are no additional impurity peaks corroborating the high purity. The characteristic peaks of CPDs are not detected from the CPDs/ZIS composites due to the small amounts and weak diffraction intensity of CPDs. However, the diffraction peak at 21.4° decreases revealing that CPDs impact the growth of ZIS. Fig. 3**b** shows two Raman scattering peaks at about 1354 and 1580 cm^{-1} attributable to the D and G bands of CPDs [43]. The D and G bands can also be observed from the 7 wt% CPDs/ZIS composite further confirming incorporation of ZIS. The FTIR spectra in Fig. 3**c** show peaks at around 3408 and 1384 cm^{-1} corresponding to hydroxyl

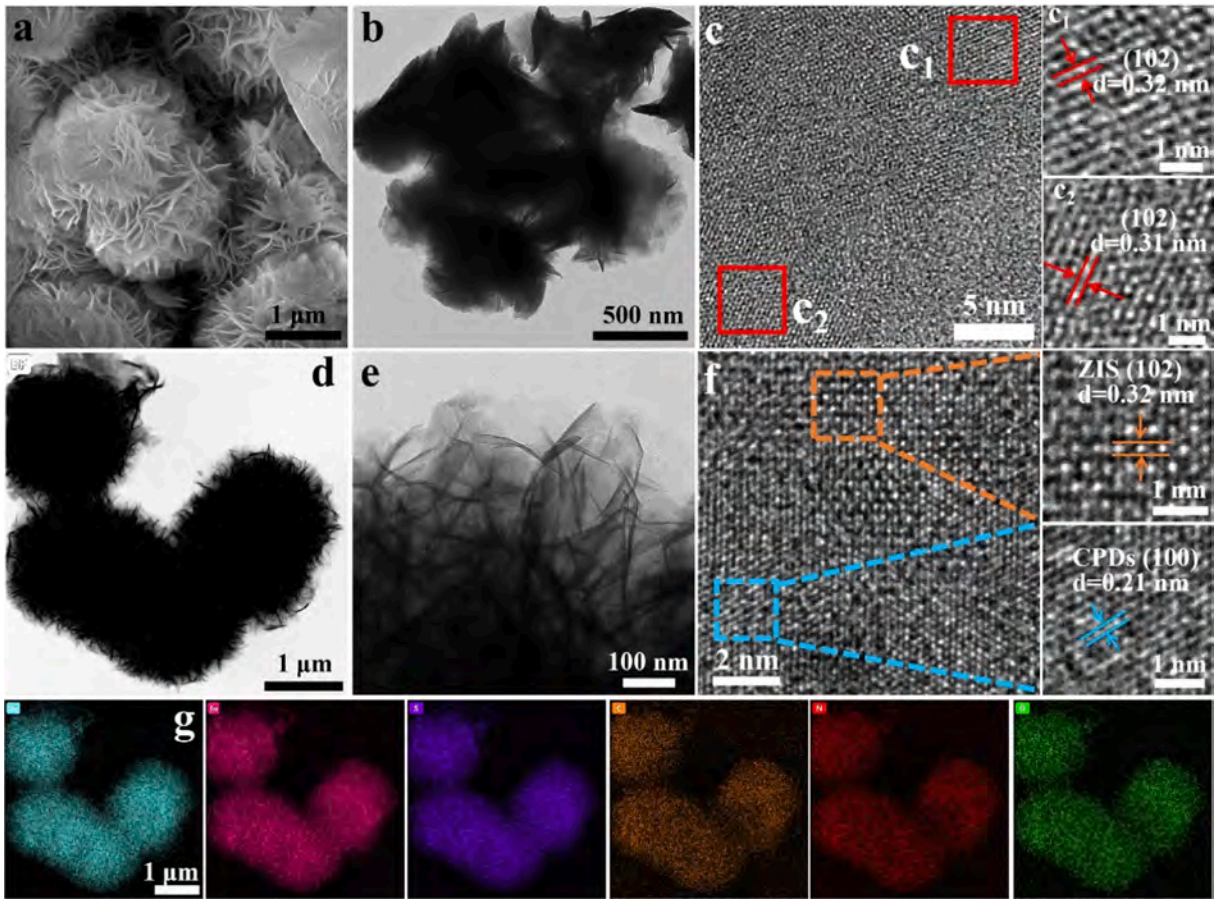

Fig. 2. (a) SEM, (b) TEM and (c) HR-TEM images of ZIS; (d, e) TEM and (f) HR-TEM images of the CPDs/ZIS composites; (g) EDS elemental maps showing Zn, In, S, C, N, and O in the CPDs/ZIS microsphere.

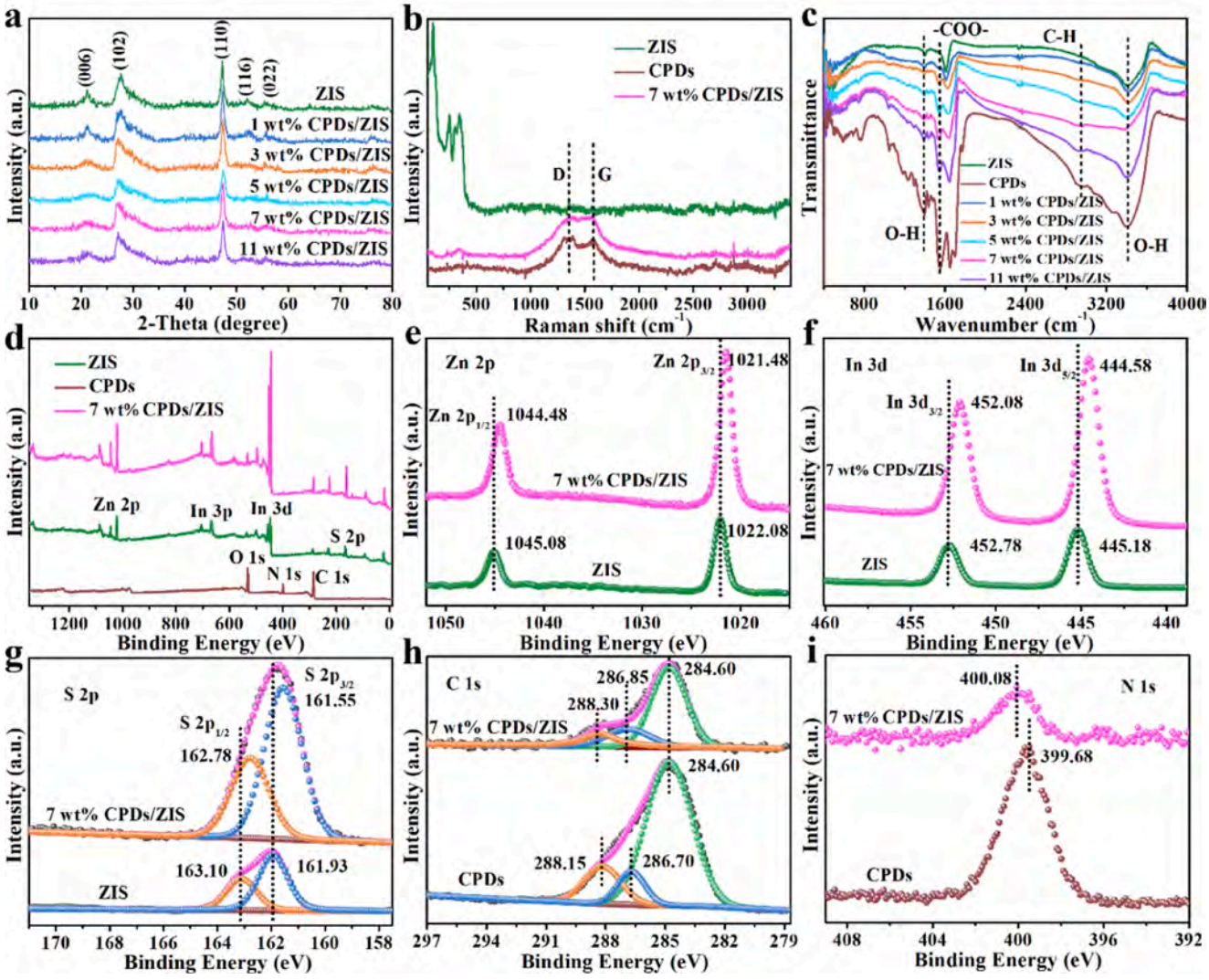

Fig. 3. (a) XRD patterns of ZIS and CPDs/ZIS; (b) Raman scattering spectra of CPDs, ZIS and 7 wt% CPDs/ZIS; (c) FTIR spectra of CPDs, ZIS, and CPDs/ZlS; (d) XPS survey spectra of ZIS, 7 wt% CPDs/ZlS, and CPDs; High-resolution XPS spectra of ZIS, CPDs, and 7 wt% CPDs/ZlS: (e) Zn 2*p*, (f) In 3*d*, (g) S 2*p*, (h) C 1*s*, and (i) N 1*s*.

groups on the CPDs [44]. The peak at 2952 cm^{-1} stems from C-H stretching of aromatic hydrocarbon [44] that that at 1553 cm^{-1} is related to –COO- stretching [45,46]. These peaks from CPDs can be observed from all the CPDs/ZIS composites verifying that CPDs are introduced to ZIS.

XPS is performed to analyze the surface chemical composition and states. The XPS survey spectra show the presence of Zn, In, S, C, N, and O in the CPDs/ZIS composites (Fig. 3**d**). The high-resolution XPS spectrum of Zn 2*p* (Fig. 3**e**) discloses peaks at 1022.08 eV and 1045.88 eV for Zn $2p_{3/2}$ and Zn $2p_{1/2}$ of Zn^{2+}, respectively. The In 3*d* spectrum exhibits two peaks at 445.18 and 452.78 eV due to In $3d_{5/2}$ and In $3d_{3/2}$, respectively (Fig. 3**f**). The two fitted peaks of S 2*p* at 161.93 and 163.10 eV in Fig. 3**g** are S $2p_{3/2}$ and S $2p_{1/2}$.[47,48]. The XPS spectrum of C 1*s* can be deconvoluted into three peaks as shown in Fig. 3**h**. The peaks at 284.60, 286.70, and 288.15 eV are assigned to C—C/C═C, C—O and C═O, respectively [49] and that at 399.68 eV belongs to N 1*s* (Fig. 3**i**). When the CPDs/ZIS heterojunction forms, the Zn 2*p*, In 3*d*, and S 2*p* peaks of the 7 wt% CPDs/ZIS exhibit negative shifts compared to the pure ZIS, indicating electron accumulation in ZIS. On the contrary, the C 1*s* and N 1*s* peaks of 7 wt% CPDs/ZIS show positive shifts compared to CPDs. The conduction band minimum of ZIS mainly consists of the In 3*d* and S 2*p* orbitals and N atoms possess single electrons in CPDs [38]. When CPDs and ZIS are in close contact, the single electrons in CPDs migrate to the conduction band of ZIS and the interfaces of ZIS and CPDs possess positive and negative charges, respectively. Therefore, the internal electric field with a direction from CPDs to ZIS forms at the contact. The work function is used to analyse the transfer of electrons in the Z-scheme heterostructures. The value of work function is the difference between the electrostatic potential in vacuum and the Fermi level. As shown in the **Fig. S2**, the work functions of ZIS, CPDs and CPDs/ZIS heterojunctions are 6.64 eV, 4.82 eV and 6.27 eV, respectively. Obviously, the Fermi levels of ZIS is lower than that of CPDs, and the Fermi level of CPDs/ZIS composites is between CPDs and ZIS. When ZIS and CPDs are in close contact, the electrons in CPDs would be transferred to ZIS to balance the Fermi level of composites and the internal electric field with the direction from CPDs to ZIS would be created [50]. The calculated results are consistent with XPS.

UV–vis absorption spectra are collected to study the optical properties as shown in Fig. 4**a**. The absorption edge of ZIS is at approximately 500 nm. All the CPDs/ZIS composites exhibit better absorption than the pristine ZIS. Moreover, the absorption edge of CPDs/ZIS red-shifts with increasing amounts of CPDs due to light absorption of CPDs boding well for the photocatalytic properties. The bandgap (E_g) of ZIS is calculated by: $\alpha h\nu = A\ (h\nu - E_g)^{n/2}$ and the $(\alpha E_{photon})^{1/2}$ versus E_{photon} curve of the ZIS monomer is determined by the Tauc approach to be about 2.36 eV (Fig. 4**b**).

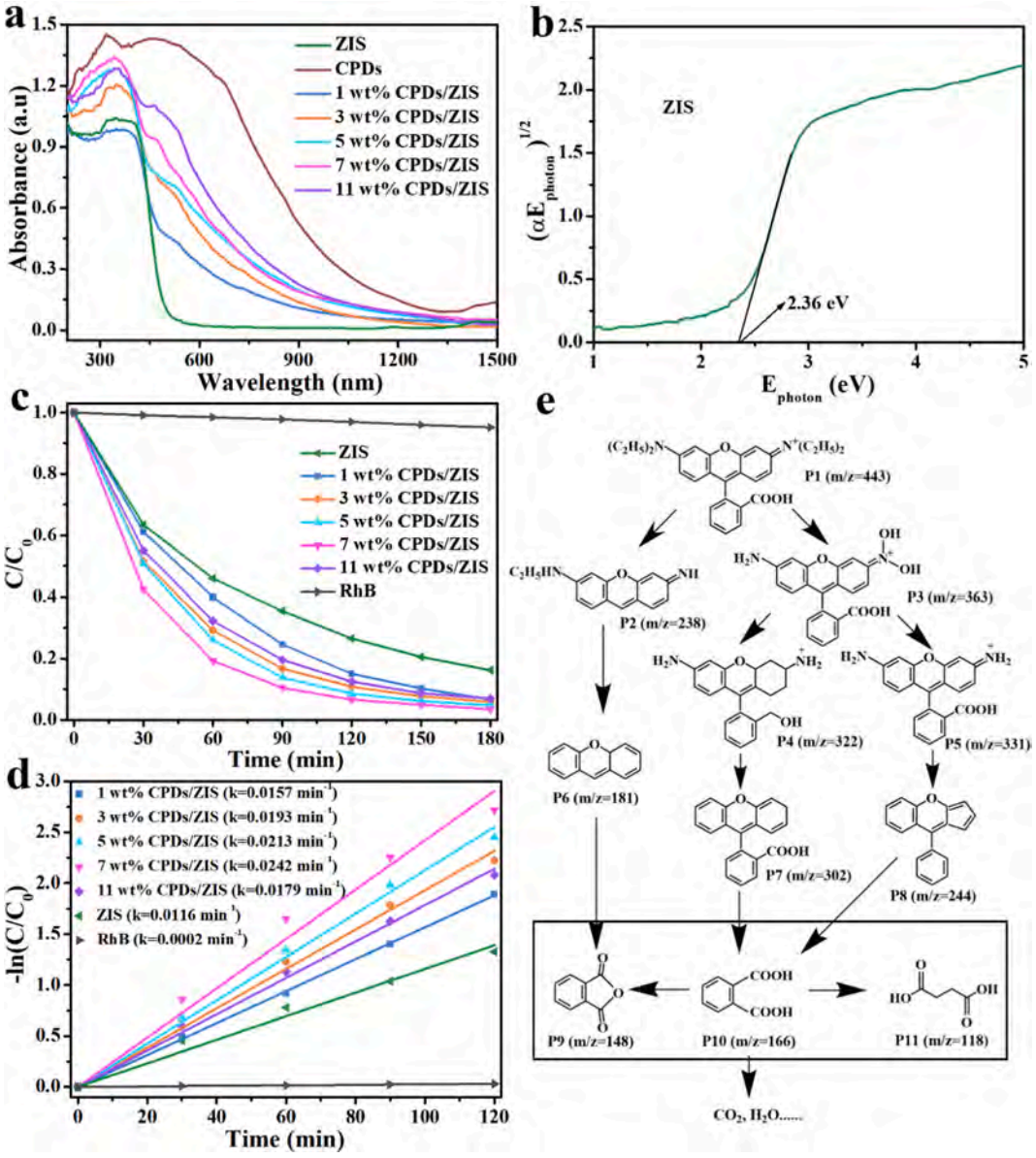

Fig. 4. (a) UV–vis DRS of the photocatalysts, (b) $(\alpha E_{photon})^{1/2}$ vs E_{photon} curves of ZIS, (c) Photocatalytic degradation curves, (d) Reaction kinetics in degradation of RhB, and (e) Degradation pathways of RhB by 7 wt% CPDs/ZIS.

RhB is a xanthene dye and widely used in the textile, paper, dyeing, and leather industry. However, it can harm skin and respiratory tracts and is carcinogenic. If industrial wastewater containing large amounts of dyes and toxic substances are disposed without proper treatment, serious pollution of surface and groundwater can result to threaten human health [51]. Herein, RhB is used to assess the photocatalytic activity of ZIS and CPDs/ZIS. As shown in Fig. 4**c**, RhB is hardly degraded without the photocatalysts. After irradiation for 3 h, the pristine ZIS removes 83 % of RhB and better results are observed from the CPDs/ZIS composites. In particular, 7 wt% CPDs/ZIS removes 97 % of RhB after illumination for 3 h. The photocatalytic performance improves first and then degrades with increasing amounts of CPDs possibly because the excess CPDs cover the active sites of ZIS. The degradation kinetics exhibits the relationship of $-\ln(C/C_0) = kt$ (k is the kinetic rate constant) (Fig. 4**d**). The rate constants of all the CPDs/ZIS composites are larger than that of ZIS with that of 7 wt% CPDs/ZIS being 2.1 times higher than that of ZIS.

To further explore the degradation process, LC-MS is used to analyze the degradation products of RhB. As shown in **Fig. S3**, many intermediates are produced and the possible pathways are deduced. As shown in Fig. 4**e**, RhB molecules adsorb on the photocatalyst *via* the diethylamine group with a positive charge. The C-N bong is attacked by $\cdot O_2^-$ and h^+ resulting in breakage to form P2 ($m/z = 238$) by N-de-ethylation and cleavage of C–C band and P3 ($m/z = 363$) by N-de-ethylation. After successive attack of $\cdot O_2^-$ and h^+, P2 is converted to P6 ($m/z = 181$) through de-amination and P3 is further converted to P4 ($m/z = 322$) and P5 ($m/z = 331$). The intermediate P7 ($m/z = 302$) is produced due to the de-amination of P4, and P8 ($m/z = 244$) is generated by de-amination and de-carboxylation reactions of P5. Afterwards, P6, P7, and P8 decompose into smaller organic molecules such as P9 ($m/z = 148$), P10 ($m/z = 166$), and P11 ($m/z = 118$) *via* chromophore cleavage and ring opening and these smaller molecules are further converted into H_2O and CO_2.

To evaluate the diversity of the photocatalysts, MBT degradation is also performed. As shown in Fig. 5**a**, after light irradiation for 3 h, only 2 % MBT is degraded in the absence of photocatalysts, indicating that MBT is difficult to degrade naturally. On the other hand, the CPDs/ZIS composites show higher photocatalytic activities in MBT removal and 7

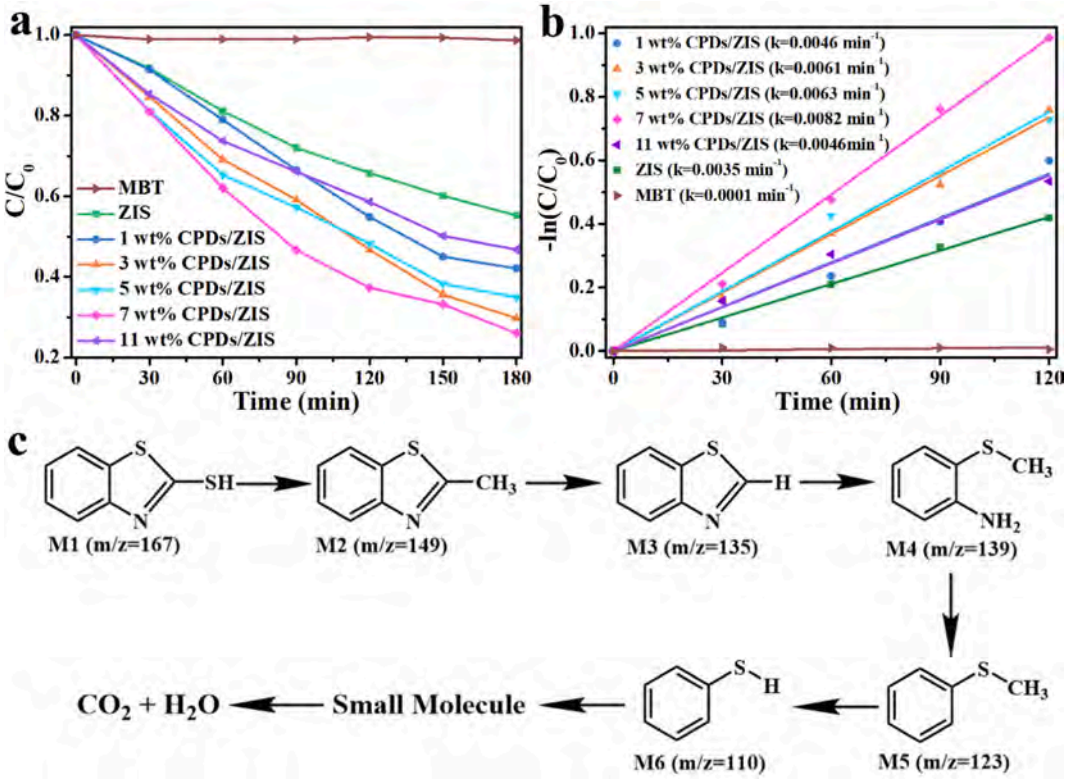

Fig. 5. (a) Photocatalytic degradation curves and (b) Reaction kinetics in degradation of MBT; (c) Degradation pathways of MBT by 7 wt% CPDs/ZIS.

wt% CPDs/ZIS is the best showing that 74 % of MBT is degraded after irradiation for 3 h, compared to 45 % for the pristine ZIS under the same conditions. The reaction kinetics of MBT degradation shows the following relationship: $\ln(C/C_0) = kt$ (k: the kinetic rate constant) (Fig. 5**b**). The rate constants of MBT, ZIS, 1 wt%, 3 wt%, 5 wt%, 7 wt% and 11 wt% CPDs/ZIS are 0.0001 min^{-1}, 0.0035 min^{-1}, 0.0046 min^{-1}, 0.0061 min^{-1}, 0.0063 min^{-1}, 0.0082 min^{-1}, and 0.0046 min^{-1}, respectively. The rate constants of all the CPDs/ZIS composites are larger than that ZIS and that of 7 wt% CPDs/ZIS is 2.3 times larger than that of ZIS.

The intermediates formed during MBT degradation are detected by MS (**Fig. S4**) and the degradation pathway is proposed. As shown in Fig. 5**c**. owing to attack by reactive oxygen species, the C-S bond in MBT breaks and is replaced by methyl groups to form the intermediate M2 (m/z = 149). M2 is converted to M3 (m/z = 135) by demethylation. Under continuous attack by reactive oxygen species, the N=C bond of M3 breaks and ring opening occurs to form the intermediate M4 (m/z = 139). M5 (m/z = 123) is generated by the de-amino reaction of M4 and M5 decomposes to form M6 (m/z = 110) via demethylation. M6 continues to break down into small molecules and eventually is mineralized into CO_2 and H_2O.

In order to compare the performance of CPDs/ZIS composites with that of other photocatalytic materials, carbon nitride (C_3N_4), zinc oxide (ZnO), titanium dioxide (TiO_2) and bismuth oxybromide (BiOBr) were selected for photocatalytic degradation experiment under the same conditions. The results are presented in Fig. S5**a**. After 3 h of light irradiation, ZnO, TiO_2 and BiOBr could only degrade about 10 % of RhB. Only 35 % of RhB can be removed by C_3N_4 after 3 h of light irradiation. On the contrary, 7 wt% CPDs/ZIS can degrade 97 % of RhB after 3 h of light irradiation. Obviously, CPDs/ZIS composites exhibit excellent photocatalytic degradation performance. To study whether the performance of photocatalyst will be affected by acidity or alkalinity, the pH values of pollutants were adjusted to be 1, 3, 5, 9, 11, 13 using 1 mol/L HCl solution and NaOH solution. As shown in the Fig. S5**b**, under the acidic conditions, the degradation efficiency of RhB has little change. However, under the alkaline conditions, the degradation efficiency of RhB increased slightly. The possible reason is that alkaline environment is conducive to the adsorption of pollutants by materials. More pollutants are adsorbed on the surface of the material, which promotes the degradation of pollutants. In addition, the effects of other ions on photocatalytic degradation were further studied. NaCl, $NaNO_3$, Na_2SO_4 and Na_2CO_3 were added into the RhB solution to study the effect of anions on the degradation reaction; NaCl, $CaCl_2$, KCl and NH_4Cl were added into the RhB solution to study the effect of cations on the degradation reaction. As shown in the **Fig. S6**, when these inorganic salts are added into the RhB solution, the degradation efficiency of RhB has no obvious change, indicating that the existence of anions and cations in the solution has no influence on the degradation reaction. Therefore, CPDs/ZIS composites possess good anti-interference performance.

EIS is carried out and the photocurrents are measured to analyze separation and transfer of carriers [52,53]. Generally, a smaller Nyquist plot diameter implies a smaller charge transfer resistance [54,55]. As shown in Fig. 6**a**, the Nyquist diameter of 7 wt% CPDs/ZIS is smaller than that of ZIS, indicating that the former has a smaller charge transfer resistance. Compared to ZIS, the CPDs/ZIS composites show higher photocurrent densities with that of 7 wt% CPDs/ZIS being 3 times higher than that of ZIS (Fig. 6**b**). Hence, a small amount of CPDs in ZIS is sufficient to promote separation of photoexcited charges. Recombination of photoexcited carriers is investigated by photoluminescence (PL) (Fig. 6**c**). The fluorescence intensity from 7 wt% CPDs/ZIS is obviously lower than that from the pristine ZIS, indicating that recombination of photoexcited carriers is prevented after introduction of CPDs. The PL spectra also suggest high photocatalytic performance of 7 wt% CPDs/ZIS. To demonstrate the stability, cycling experiments are conducted as shown in **Fig. S7a**. After nine cycles, the photocatalytic degradation properties of 7 wt% CPDs/ZIS decrease only slightly and **Fig. S7b** and **Fig. S7c** confirm good structural stability after cycling.

The active species are detected by ESR and free radicals capturing experiments [56]. As shown in Fig. 6**d and e**, without light irradiation, no signals of DMPO-·O_2^- and DMPO-·OH are observed from ZIS and 7 wt

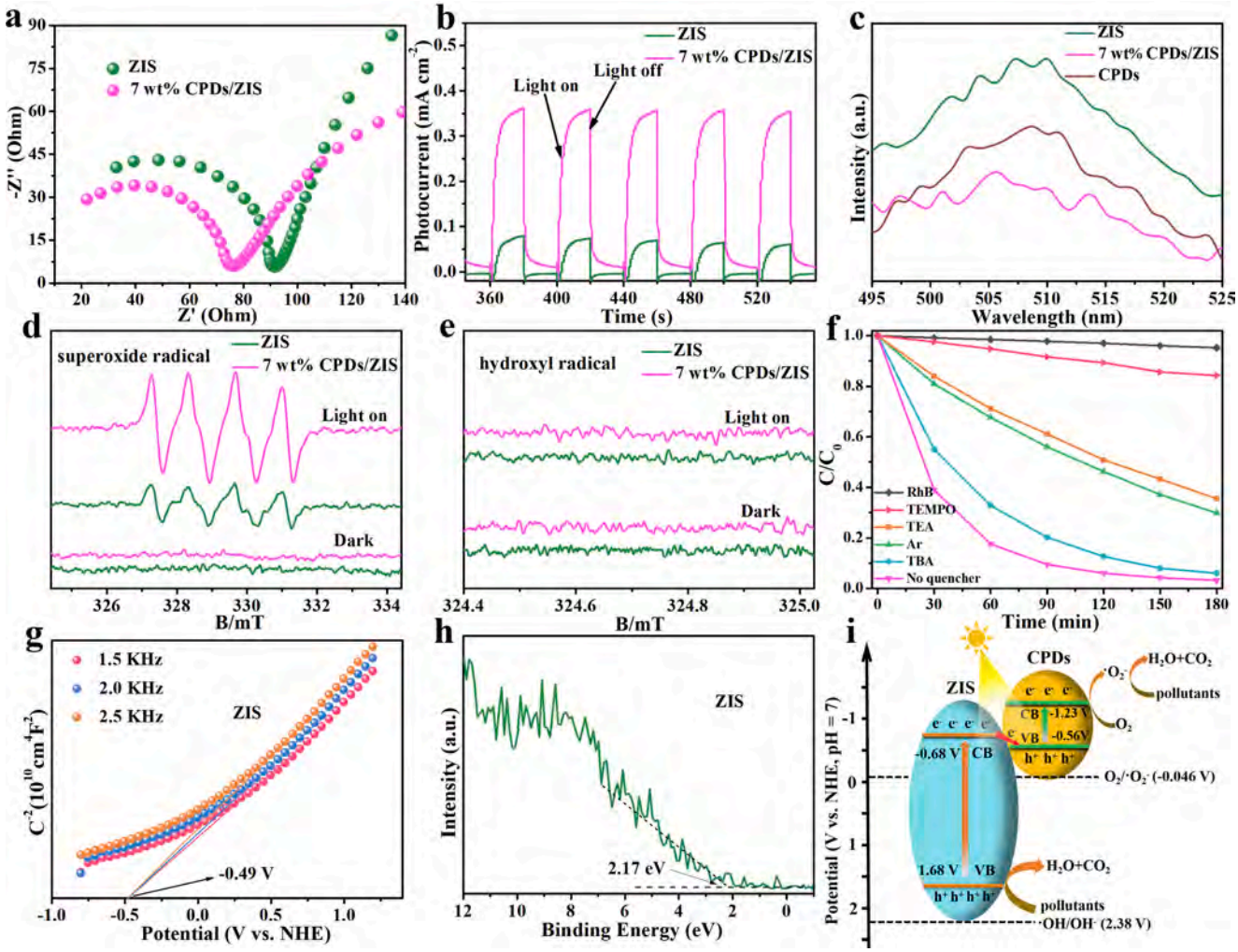

Fig. 6. (a) EIS spectra, (b) Photocurrents, and (c) PL spectra of ZIS and 7 wt% CPDs/ZIS; ESR spectra of (d) DMPO-·O_2^- and (e) DMPO-·OH of ZIS and 7 wt% CPDs/ZIS; (f) Trapping experiments of active species; (g) Mott-Schottky plots of ZIS; (h) XPS valence-band spectrum of ZIS; (i) Schematic illustration of the mechanism of 7 wt% CPDs/ZIS.

% CPDs/ZIS, indicate that no reactive oxygen species are generated without light. Upon light irradiation, both ZIS and 7 wt% CPDs/ZIS show the signal of DMPO-·O_2^-, and that from 7 wt% CPDs/ZIS is obviously stronger than from of ZIS, indicating that more ·O_2^- is produced by 7 wt% CPDs/ZIS. However, the peaks of DMPO-·OH cannot be observed from ZIS and 7 wt% CPDs/ZIS (Fig. 6**e**) because the VB position of ZIS is more negative than that of OH/OH^- (2.38 V vs. NHE). Therefore, OH^- cannot be converted to ·OH by holes in the VB of ZIS. Capturing experiments are performed to determine the reactive species. Triethanolamine (TEA), *tert*-butyl alcohol (TBA), and TEMPO are quenching agents for h^+, ·OH, and ·O_2^-, respectively. In addition, introducing argon (Ar) into the reaction can prevent the generation of oxygen active species. The photocatalytic activity of 7 wt% CPDs/ZIS does not change after addition of TBA, but that of RhB decreases after adding TEA and TEMPO (Fig. 6**f**), indicating that h^+ and ·O_2^- play important roles in photocatalytic degradation. The capturing experiments demonstrate that ·O_2^- and h^+ are the main active species in 7 wt% CPDs/ZIS for degradation of RhB in line with ESRs.

The band structure of ZIS is investigated by the Mott-Schottky curve and XPS valence band spectrum. The Mott-Schottky curve of ZIS is displayed in Fig. 6**g**. Generally, a tangent line is made for the longest straight line in the Mott-Schottky curve. If the slope of the tangent line is positive, it is an n-type semiconductor. Obviously, ZIS is an n-type semiconductor and the flat band potential is −0.49 V. Previous studies have demonstrated the flat band potential of a n-type semiconductor is approximately equal to its Fermi level. The XPS valence band is 2.17 eV (Fig. 6**h**) and the VB of ZIS is calculated to be 1.68 V. According to $E_{CB} = E_{VB} - E_g$, the CB of ZIS is calculated to be −0.68 V. The VB and CB of CPDs have been reported to be −0.56 and −1.23 V, respectively [38].

Based on the band structures of ZIS and CPDs, the photocatalytic mechanism of CPDs/ZIS is proposed. As shown in Fig. 6**i**, electrons in the VB of both ZIS and CPDs are excited and transition to the CB due to the light irradiation. Under the effects of the internal electric field between CPDs and ZIS, electrons in the CB of ZIS combine with holes in the VB of CPDs through the Z-scheme structure. The holes in the VB of ZIS and electrons in the CB of CPDs are retained giving rise to effective separation of photo-induced electron-hole pairs. Since the valence band position of ZIS is more negative than that of E^0 (·OH/OH^-) (2.38 eV vs. NHE), holes in the valence band of ZIS cannot oxidize OH^- to ·OH, whereas holes can directly oxidize pollutants. The conduction band position of CPDs is higher than $E^0(O_2/\cdot O_2^-) = -0.046$ eV vs. NHE). Therefore, electrons in the CB of CPDs can reduce O_2 and generate more reactive oxygen species ·O_2^-. Under the combined effects of h^+ and ·O_2^-, pollutants decompose gradually into H_2O and CO_2. In this process, CPDs play a crucial role in the photocatalytic activity. Owing to the confinement effects of CPDs, a large number of electrons accumulate on CPDs to become local active sites and generate more ·O_2^-. In addition, spatial separation of electrons and holes allows more holes in the valence band

of ZIS to be retained and more superoxide radicals and holes improve photocatalytic degradation.

4. Conclusion

Flower-like direct Z-scheme CPDs/ZIS photocatalysts are designed and demonstrated. The Z-scheme mechanism exploits directional migration of photogenerated charges and more holes in the valence band of ZIS are retained to participate in degradation. Because of the confinement effects of CPDs, a large number of photogenerated electrons accumulate on CPDs and more oxygen is reduced to generate superoxide radicals. As a result, the photocatalytic activity of the CPDs/ZIS composites is enhanced significantly. In particular, 7 wt% CPDs/ZIS delivers the best performance in degradation of RhB and MBT under visible light irradiation and the rates are 2.1 times and 2.4 times higher than those of pristine ZIS. ESR and radicals trapping experiments show that h^+ and $\cdot O_2^-$ play important roles in the degradation process. The photocatalytic mechanism and pathways are analyzed and determined. The results reveal directional migration of photogenerated charges in the Z-scheme heterojunctions and confinement effects of carbonized polymer dots and provide insights into the development cost-effective and efficient photocatalysts.

CRediT authorship contribution statement

Xingwang Yan: Conceptualization, Data curation, Investigation, Writing – original draft. **Xiaolin Zhang:** Data curation, Investigation, Writing – original draft. **Bin Wang:** Data curation, Investigation. **Ziran Chen:** Software, Validation. **Junze Zhao:** Software, Validation. **Gaopeng Liu:** Data curation, Investigation. **Dan Li:** Resources, Supervision. **Qingdong Ruan:** Resources, Writing – review & editing, Supervision. **Liangliang Liu:** Data curation, Investigation. **Yue Xu:** Data curation, Investigation. **Mengxia Ji:** Data curation, Investigation. **Paul K. Chu:** Resources, Writing – review & editing, Supervision. **Huaming Li:** Resources, Writing – review & editing, Supervision. **Jiexiang Xia:** Conceptualization, Resources, Writing – review & editing, Supervision.

Declaration of Competing Interest

The authors declare that they have no known competing financial interests or personal relationships that could have appeared to influence the work reported in this paper.

Data availability

Data will be made available on request.

Acknowledgments

This work was financially supported by the National Natural Science Foundation of China (No. 22108106, 22108108, 22108055, 21676128), Natural Science Foundation of Jiangsu Province (BK20210742), China Postdoctoral Science Foundation (No. 2020M680065), Hong Kong Scholars Program (XJ2021021), City University of Hong Kong Donation Research Grant (DON-RMG 9229021), City University of Hong Kong Donation Grant (9220061), as well as Hong Kong ITC (Innovation and Technology Commission) ITF (Innovation and Technology Fund) (GHP/149/20SZ and CityU 9440296).

Appendix A. Supplementary material

Supplementary data to this article can be found online at https://doi.org/10.1016/j.apsusc.2022.155782.

References

[1] Q. Guo, C. Zhou, Z. Ma, X. Yang, Fundamentals of TiO_2 Photocatalysis: Concepts, Mechanisms, and Challenges, Adv. Mater. 31 (2019) 1901997, https://doi.org/10.1002/adma.201901997.
[2] Q. Wang, K. Domen, Particulate Photocatalysts for Light-Driven Water Splitting: Mechanisms, Challenges, and Design Strategies, Chem. Rev. 120 (2020) 919–985, https://doi.org/10.1021/acs.chemrev.9b00201.
[3] S. Sun, L. He, M. Yang, J. Cui, S. Liang, Facet Junction Engineering for Photocatalysis: A Comprehensive Review on Elementary Knowledge, Facet-Synergistic Mechanisms, Functional Modifications, and Future Perspectives, Adv. Funct. Mater. 32 (2022) 2106982, https://doi.org/10.1002/adfm.202106982.
[4] M. Xiao, Z. Wang, M. Lyu, B. Luo, S. Wang, G. Liu, H. Cheng, L. Wang, Hollow Nanostructures for Photocatalysis: Advantages and Challenges, Adv. Mater. 31 (2019) 1801369, https://doi.org/10.1002/adma.201801369.
[5] B. Pan, Y. Wu, B. Rhimi, J. Qin, Y. Huang, M. Yuan, C. Wang, Oxygen-doping of $ZnIn_2S_4$ nanosheets towards boosted photocatalytic CO_2 reduction, J. Energy Chem. 57 (2021) 1–9, https://doi.org/10.1016/j.jechem.2020.08.024.
[6] J. Fu, J. Yu, C. Jiang, B. Cheng, g-C_3N_4-Based Heterostructured Photocatalysts, Adv. Energy Mater. 8 (2018) 1701503, https://doi.org/10.1002/aenm.201701503.
[7] L. Cheng, H. Zhang, X. Li, J. Fan, Q. Xiang, Carbon-Graphitic Carbon Nitride Hybrids for Heterogeneous Photocatalysis, Small 17 (2021) 2005231, https://doi.org/10.1002/smll.202005231.
[8] J. Di, C. Chen, C. Zhu, P. Song, M. Duan, J. Xiong, R. Long, M. Xu, L. Kang, S. Guo, S. Chen, H. Chen, Z. Chi, Y. Weng, H. Li, L. Song, M. Wu, Q. Yan, S. Li, Z. Liu, Cobalt nitride as a novel cocatalyst to boost photocatalytic CO_2 reduction, Nano Energy 79 (2021), 105429, https://doi.org/10.1016/j.nanoen.2020.105429.
[9] S. Khan, H. Choi, D. Kim, S. Lee, Q. Zhu, J. Zhang, S. Kim, S. Cho, Self-assembled heterojunction of metal sulfides for improved photocatalysis, Chem. Eng. J. 395 (2020), 125092, https://doi.org/10.1016/j.cej.2020.125092.
[10] T. Lange, S. Reichenberger, S. Ristig, M. Rohe, J. Strunk, S. Barcikowski, R. Schlogl, Zinc sulfide for photocatalysis: White angel or black sheep? Prog. Mater. Sci. 124 (2022), 100865 https://doi.org/10.1016/j.pmatsci.2021.100865.
[11] N. Tian, C. Hu, J. Wang, Y. Zhang, T. Ma, H. Huang, Layered bismuth-based photocatalysts, Coord. Chem. Rev. 463 (2022), 214515, https://doi.org/10.1016/j.ccr.2022.214515.
[12] S. Wang, L. Wang, W. Huang, Bismuth-Based Photocatalysts for Solar Energy Conversion, J. Mater. Chem. A 46 (2020) 1–109, https://doi.org/10.1039/D0TA09729B.
[13] H. Zhu, X. Yuan, Q. Yao, J. Xie, Shining photocatalysis by gold-based nanomaterials, Nano Energy 88 (2021), 106306, https://doi.org/10.1016/j.nanoen.2021.106306.
[14] C. Du, B. Yan, G. Yang, Promoting photocatalytic hydrogen evolution by introducing hot islands: SnSe nanoparticles on $ZnIn_2S_4$ monolayer, Chem. Eng. J. 404 (2021), 126477, https://doi.org/10.1016/j.cej.2020.126477.
[15] W. Yang, X.L. Wang, N. Kong, C. Liu, P. Sun, Z. Wang, Y. Ding, H. Lin, D. Li, T. Wu, Minimized external electric field on asymmetric monolayer maximizes charge separation for photocatalysis, Appl. Catal. B 295 (2021) 120266, https://doi.org/10.1016/j.apcatb.2021.120266.
[16] B. Wang, W. Zhang, G. Liu, H. Chen, Y. Weng, H. Li, P.K. Chu, J. Xia, Excited electron-rich $Bi^{(3-x)+}$ sites: a quantum well-like structure for highly-promoted selective photocatalytic CO_2 reduction performance, Adv. Funct. Mater. 32 (2022) 202202885, https://doi.org/10.1002/adfm.202202885.
[17] P. Zhang, Y. Li, Y. Zhang, R. Hou, X. Zhang, C. Xue, S. Wang, B. Zhu, N. Li, G. Shao, Photogenerated Electron Transfer Process in Heterojunctions: In Situ Irradiation XPS, Small Methods 4 (2020) 2000214, https://doi.org/10.1002/smtd.202000214.
[18] R. Hou, S. Zhang, Y. Zhang, N. Li, S. Wang, B. Ding, G. Shao, P. Zhang, A "Three-Region" Configuration for Enhanced Electrochemical Kinetics and High-Areal Capacity Lithium-Sulfur Batteries, Adv. Funct. Mater. 32 (2022) 2200302, https://doi.org/10.1002/adfm.202200302.
[19] L. Zhang, J. Zhang, H. Yu, J. Yu, Emerging S-Scheme Photocatalyst, Adv. Mater. 34 (2022) 2107668, https://doi.org/10.1002/adma.202107668.
[20] M. Qin, W. Fu, H. Guo, C. Niu, D. Huang, C. Liang, Y. Yang, H. Liu, N. Tang, Q. Fan, 2D/2D Heterojunction systems for the removal of organic pollutants: A review, Adv. Colloid Interface Sci. 297 (2021), 102540, https://doi.org/10.1016/j.cis.2021.102540.
[21] Y. He, J. Shi, Q. Yang, Y. Tong, Z. Ma, L. Junior, B. Yao, Co-doped 3D petal-like $ZnIn_2S_4$/GaN heterostructures for efficient removal of chlortetracycline residue from real pharmaceutical wastewater, Chem. Eng. J. 446 (2022), 137355, https://doi.org/10.1016/j.cej.2022.137355.
[22] W. Gao, L. Wang, C. Gao, J. Liu, Y. Yang, L. Yang, Q. Shen, C. Wu, Y. Zhou, Z. Zou, Exquisite Design of Porous Carbon Microtubule-Scaffolding Hierarchical In_2O_3-$ZnIn_2S_4$ Heterostructures toward Efficiently Photocatalytic Conversion of CO_2 into CO, Nanoscale 12 (2020) 14676–14681, https://doi.org/10.1039/C9NR10959E.
[23] Q. Li, Y. Xia, C. Yang, K. Lv, M. Lei, M. Li, Building a direct Z-scheme heterojunction photocatalyst by $ZnIn_2S_4$ nanosheets and TiO_2 hollowspheres for highly-efficient artificial photosynthesis, Chem. Eng. J. 349 (2018) 287–296, https://doi.org/10.1016/j.cej.2018.05.094.
[24] P. Wang, Z. Shen, Y. Xia, H. Wang, L. Zheng, W. Xi, S. Zhan, Atomic Insights for Optimum and Excess Doping in Photocatalysis: A Case Study of Few-Layer Cu-$ZnIn_2S_4$, Adv. Funct. Mater. 29 (2019) 1807013, https://doi.org/10.1002/adfm.201807013.
[25] H. Fan, Y. Jin, K. Liu, W. Liu, One-Step MOF-Templated Strategy to Fabrication of Ce-Doped $ZnIn_2S_4$ Tetrakaidecahedron Hollow Nanocages as an Efficient

Photocatalyst for Hydrogen Evolution, Adv. Sci. 9 (2022) 2104579, https://doi.org/10.1002/advs.202104579.
[26] Y. Pan, X. Yuan, L. Jiang, H. Yu, J. Zhang, H. Wang, R. Guan, G. Zeng, Recent advances in synthesis, modification and photocatalytic applications of micro/nano-structured zinc indium sulfide, Chem. Eng. J. 354 (2018) 407–431, https://doi.org/10.1016/j.cej.2018.08.028.
[27] Y. Gao, B. Xu, M. Cherif, H. Yu, Q. Zhang, F. Vidal, X. Wang, F. Ding, Y. Sun, D. Ma, Y. Bi, Z. Xu, Atomic insights for Ag Interstitial/Substitutional doping into $ZnIn_2S_4$ nanoplates and intimate coupling with reduced graphene oxide for enhanced photocatalytic hydrogen production by water splitting, Appl. Catal. B 279 (2020) 119403, https://doi.org/10.1016/j.apcatb.2020.119403.
[28] J. Qiu, M. Li, J. Xu, X. Zhang, J. Yao, Bismuth sulfide bridged hierarchical Bi_2S_3/BiOCl@$ZnIn_2S_4$ for efficient photocatalytic Cr(VI) reduction, J. Hazard. Mater. 389 (2020), 121858, https://doi.org/10.1016/j.jhazmat.2019.121858.
[29] Y. Chao, P. Zhou, J. Lai, W. Zhang, H. Yang, S. Lu, H. Chen, K. Yin, M. Li, L. Tao, C. Shang, M. Tong, S. Guo, $Ni_{1-x}Co_xSe_2$-C/$ZnIn_2S_4$ Hybrid Nanocages with Strong 2D/2D Hetero-Interface Interaction Enable Efficient H_2-Releasing Photocatalysis, Adv. Funct. Mater. 31 (2021) 2100923, https://doi.org/10.1002/adfm.202100923.
[30] C. Ouyang, X. Quan, C. Zhang, Y. Pan, X. Li, Z. Hong, M. Zhi, Direct Z-scheme $ZnIn_2S_4$@MoO_3 heterojunction for efficient photodegradation of tetracycline hydrochloride under visible light irradiation, Chem. Eng. J. 424 (2021), 130510, https://doi.org/10.1016/j.cej.2021.130510.
[31] A. Sabbah, I. Shown, M. Qorbani, F.Y. Fu, T.Y. Lin, H.L. Wu, P.W. Chung, C.I. Wu, S.R.M. Santiago, J.L. Shen, K.H. Chen, L.C. Chen, Boosting photocatalytic CO_2 reduction in a ZnS/$ZnIn_2S_4$ heterostructure through strain-induced direct Z-scheme and a mechanistic study of molecular CO_2 interaction thereon, Nano Energy 93 (2022), 106809, https://doi.org/10.1016/j.nanoen.2021.106809.
[32] J. Hu, C. Chen, Y. Zheng, G. Zhang, C. Guo, C. Li, Spatially Separating Redox Centers on Z-Scheme $ZnIn_2S_4$/$BiVO_4$ Hierarchical Heterostructure for Highly Efficient Photocatalytic Hydrogen Evolution, Small 16 (2020) 2002988, https://doi.org/10.1002/smll.202002988.
[33] X. Wang, X. Wang, J. Huang, S. Li, A. Meng, Z. Li, Interfacial chemical bond and internal electric field modulated Z-scheme Sv-$ZnIn_2S_4$/$MoSe_2$ photocatalyst for efficient hydrogen evolution, Nat. Commun. 12 (2021) 4112, https://doi.org/10.1038/s41467-021-24511-z.
[34] Q. Zhang, F. Yang, S. Zhou, N. Bao, Z. Xu, M. Chaker, D. Ma, Broadband photocatalysts enabled by 0D/2D heterojunctions of nearinfrared quantum dots/graphitic carbon nitride nanosheets, Appl. Catal. B 270 (2020) 118879, https://doi.org/10.1016/j.apcatb.2020.118879.
[35] B. Wang, J. Di, L. Lu, S. Yan, G. Liu, Y. Ye, H. Li, W. Zhu, H. Li, J. Xia, Sacrificing ionic liquid-assisted anchoring of carbonized polymer dots on perovskite-like $PbBiO_2Br$ for robust CO_2 photoreduction, Appl. Catal. B 254 (2019) 551–559, https://doi.org/10.1016/j.apcatb.2019.04.068.
[36] M. Preeyanghaa, V. Vinesh, P. Sabarikirishwaran, A. Rajkamal, M. Ashokkumar, B. Neppolian, Investigating the role of ultrasound in improving the photocatalytic ability of CQD decorated boron-doped g-C_3N_4 for tetracycline degradation and first-principles study of nitrogen-vacancy formation, Carbon 192 (2022) 405–417, https://doi.org/10.1016/j.carbon.2022.03.011.
[37] W. Shi, C. Hao, Y. Fu, F. Guo, Y. Tang, X. Yan, Enhancement of synergistic effect photocatalytic/persulfate activation for degradation of antibiotics by the combination of photo-induced electrons and carbon dots, Chem. Eng. J. 433 (2022), 133741, https://doi.org/10.1016/j.cej.2021.133741.
[38] B. Wang, J. Zhao, H. Chen, Y.X. Weng, H. Tang, Z. Chen, W. Zhu, Y. She, J. Xia, H. Li, Unique Z-scheme carbonized polymer dots/$Bi_4O_5Br_2$ hybrids for efficiently boosting photocatalytic CO_2 reduction, Appl. Catal. B 293 (2021) 120182, https://doi.org/10.1016/j.apcatb.2021.120182.
[39] S. Wang, B. Guan, X.W.D. Lou, Construction of $ZnIn_2S_4$-In_2O_3 Hierarchical Tubular Heterostructures for Efficient CO_2 Photoreduction, J. Am. Chem. Soc. 140 (2018) 5037–5040, https://doi.org/10.1021/jacs.8b02200.
[40] Q. Liang, W. Gao, C. Liu, S. Xu, Z. Li, A novel 2D/1D core-shell heterostructures coupling MOF-derived iron oxides with $ZnIn_2S_4$ for enhanced photocatalytic activity, J. Hazard. Mater. 392 (2020), 122500, https://doi.org/10.1016/j.jhazmat.2020.122500.
[41] B. Liu, X. Liu, L. Li, J. Li, C. Li, Y. Gong, L. Niu, X. Zhao, C. Sun, $ZnIn_2S_4$ flowerlike microspheres embedded with carbon quantum dots for efficient photocatalytic reduction of Cr(VI), Chin. J. Catal. 39 (2018) 1901–1909, https://doi.org/10.1016/S1872-2067(18)63137-7.
[42] X. Wang, J. Chen, Q. Li, L. Li, Z. Zhuang, F. Chen, Y. Yu, Light-Driven Syngas Production over Defective $ZnIn_2S_4$ Nanosheets, Chem. Eur. J. 27 (2021) 3786–3792, https://doi.org/10.1002/chem.202004520.
[43] Q. Li, C. Cui, H. Meng, J. Yu, Visible-Light Photocatalytic Hydrogen Production Activity of $ZnIn_2S_4$ Microspheres Using Carbon Quantum Dots and Platinum as Dual Cocatalysts, Chem. Asian J. 9 (2014) 1766–1770, https://doi.org/10.1002/asia.201402128.
[44] H. Xu, Y. Jiang, X. Yang, F. Li, A. Li, Y. Liu, J. Zhang, Z. Zhou, L. Ni, Fabricating carbon quantum dots doped $ZnIn_2S_4$ nanoflower composites with broad spectrum and enhanced photocatalytic Tetracycline hydrochloride degradation, Mater. Res. Bull. 97 (2018) 158–168, https://doi.org/10.1016/j.materresbull.2017.09.004.
[45] B. Wang, Z. Deng, Z. Li, Efficient chemoselective hydrogenation of nitrobenzene to aniline, azoxybenzene and azobenzene over CQDs/$ZnIn_2S_4$ nanocomposites under visible light, J. Catal. 389 (2020) 241–246, https://doi.org/10.1016/j.jcat.2020.05.041.
[46] Y.H. Gao, X.H. Ji, D. Zhang, Z.F. Liu, J.F. Lu, Microwave-assisted fabrication of CQDs/$ZnIn_2S_4$ nanocomposites for synergistic photocatalytic removal of Cr(VI) and rhodamine B, Inorg. Nano-Met. Chem. 51 (2021) 451–457, https://doi.org/10.1080/24701556.2020.1862210.
[47] S. Zhang, X. Liu, C. Liu, S. Luo, L. Wang, T. Cai, Y. Zeng, J. Yuan, W. Dong, Y. Pei, Y. Liu, MoS_2 Quantum Dot Growth Induced by S Vacancies in a $ZnIn_2S_4$ Monolayer: AtomicLevel Heterostructure for Photocatalytic Hydrogen Production, ACS Nano 12 (2018) 751–758, https://doi.org/10.1021/acsnano.7b07974.
[48] X. Ye, T. Zhu, Z. Hui, X. Wang, J. Wei, S. Chen, Revealing the transfer mechanisms of photogenerated charge carriers over g-C_3N_4/$ZnIn_2S_4$ composite: A model study for photocatalytic oxidation of aromatic alcohols with visible light, J. Catal. 401 (2021) 149–159, https://doi.org/10.1016/j.jcat.2021.07.025.
[49] Y. Ding, Y. Gao, Z. Li, Carbon quantum dots (CQDs) and Co$(dmgH)_2$PyCl synergistically promote photocatalytic hydrogen evolution over hexagonal $ZnIn_2S_4$, Appl. Surf. Sci. 462 (2018) 255–262, https://doi.org/10.1016/j.apsusc.2018.08.006.
[50] Y. Xi, W. Chen, W. Dong, Z. Fan, K. Wang, Y. Shen, G. Tu, S. Zhong, S. Bai, Engineering an Interfacial Facet of S-Scheme Heterojunction for Improved Photocatalytic Hydrogen Evolution by Modulating the Internal Electric Field, ACS Appl. Mater. Interfaces 13 (2021) 39491–39500, https://doi.org/10.1021/acsami.1c11233.
[51] H. Luo, J. Guo, T. Shen, H. Zhou, J. Liang, S. Yuan, Study on the catalytic performance of $LaMnO_3$ for the RhB degradation, J. Taiwan Inst. Chem. Eng. 109 (2020) 15–25, https://doi.org/10.1016/j.jtice.2020.01.011.
[52] G. Liu, L. Wang, X. Chen, X. Zhu, B. Wang, X. Xu, Z. Chen, W. Zhu, H. Li, J. Xia, Crafting of plasmonic Au nanoparticles coupled ultrathin BiOBr nanosheets heterostructure: steering charge transfer for efficient CO_2 photoreduction, Green Chem. Eng. 3 (2022) 157–164, https://doi.org/10.1016/j.gce.2021.11.007.
[53] J. Dong, F. Chen, L. Xu, P. Yan, J. Qian, Y. Chen, M. Yang, H. Li, Fabrication of sensitive photoelectrochemical aptasensor using Ag nanoparticles sensitized bismuth oxyiodide for determination of chloramphenicol, Microchem. J. 178 (2022), 107317, https://doi.org/10.1016/j.microc.2022.107317.
[54] L. Wang, Y. Li, C. Wu, X. Li, G. Shao, P. Zhang, Tracking charge transfer pathways in $SrTiO_3$/CoP/Mo_2C nanofibers for enhanced photocatalytic solar fuel production, Chin. J. Catal. 43 (2022) 507–518, https://doi.org/10.1016/S1872-2067(21)63898-6.
[55] Y. Zhang, P. Zhang, S. Zhang, Z. Wang, N. Li, S.R.P. Silva, G. Shao, A flexible metallic TiC nanofiber/vertical graphene 1D/2D heterostructured as active electrocatalyst for advanced Li-S batteries, InfoMat. 3 (2021) 790–803, https://doi.org/10.1002/inf2.12214.
[56] Y. Li, H. Dong, L. Li, J. Xiao, S. Xiao, Z. Jin, Efficient degradation of sulfamethazine via activation of percarbonate by chalcopyrite, Water Res. 202 (2021), 117451, https://doi.org/10.1016/j.watres.2021.117451.

Supporting Information

Confinement effects of carbonized polymer dots and directional migration of $ZnIn_2S_4$ photogenerated charge carriers for enhanced water purification

Xingwang Yan[a], Xiaolin Zhang[b], Bin Wang[a,b], Ziran Chen[c], Junze Zhao[a], Gaopeng Liu[a], Dan Li[b], Qingdong Ruan[b], Liangliang Liu[b], Yue Xu[b], Mengxia Ji[a], Paul K. Chu[b], Huaming Li[a], Jiexiang Xia[a,*]

[a] *School of Chemistry and Chemical Engineering, Institute for Energy Research, Jiangsu University, 301 Xuefu Road, Zhenjiang 212013, China*

[b] *Department of Physics, Department of Materials Science and Engineering, and Department of Biomedical Engineering, City University of Hong Kong, Tat Chee Avenue, Kowloon, Hong Kong, China*

[c] *Department of Architecture and Environment Engineering, Sichuan Vocational and Technical College, Suining 629000, Sichuan, China*

E-mail: xjx@ujs.edu.cn (J. X. Xia)

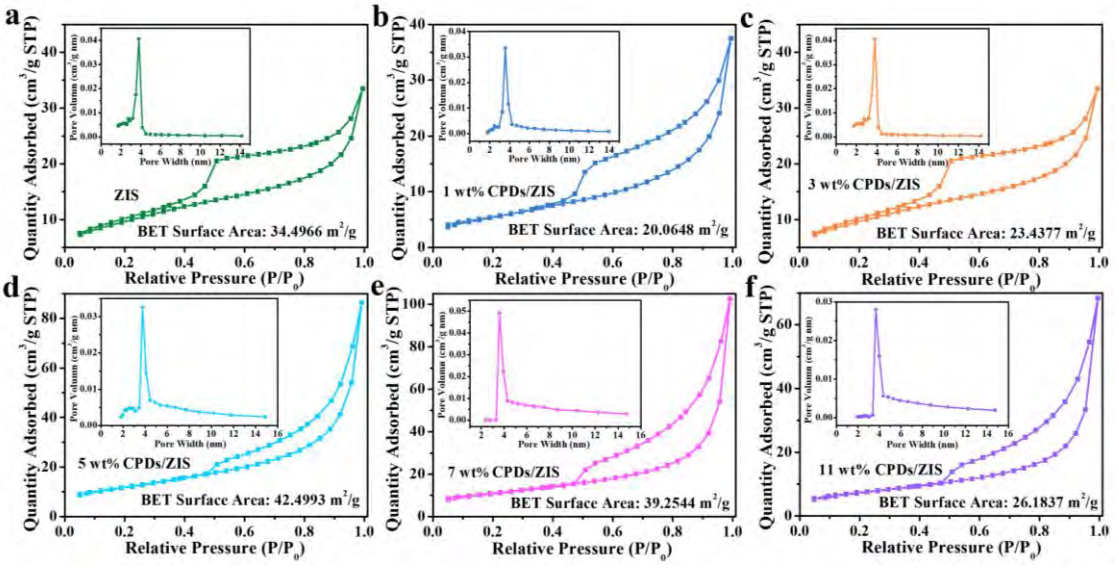

Fig. S1 Nitrogen absorption-desorption isotherms of (a) ZIS, (b) 1 wt%, (c) 3 wt%, (d) 5 wt% (e) 7 wt%, (f) 11 wt% CPDs/ZIS composite materials.

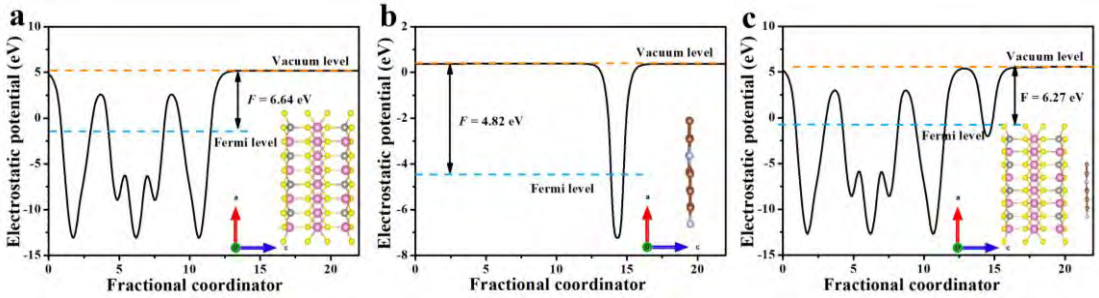

Fig. S2 The calculated work function and corresponding structural model of the (a) ZIS, (b) CPDs and (c) CPDs/ZIS heterojunction.

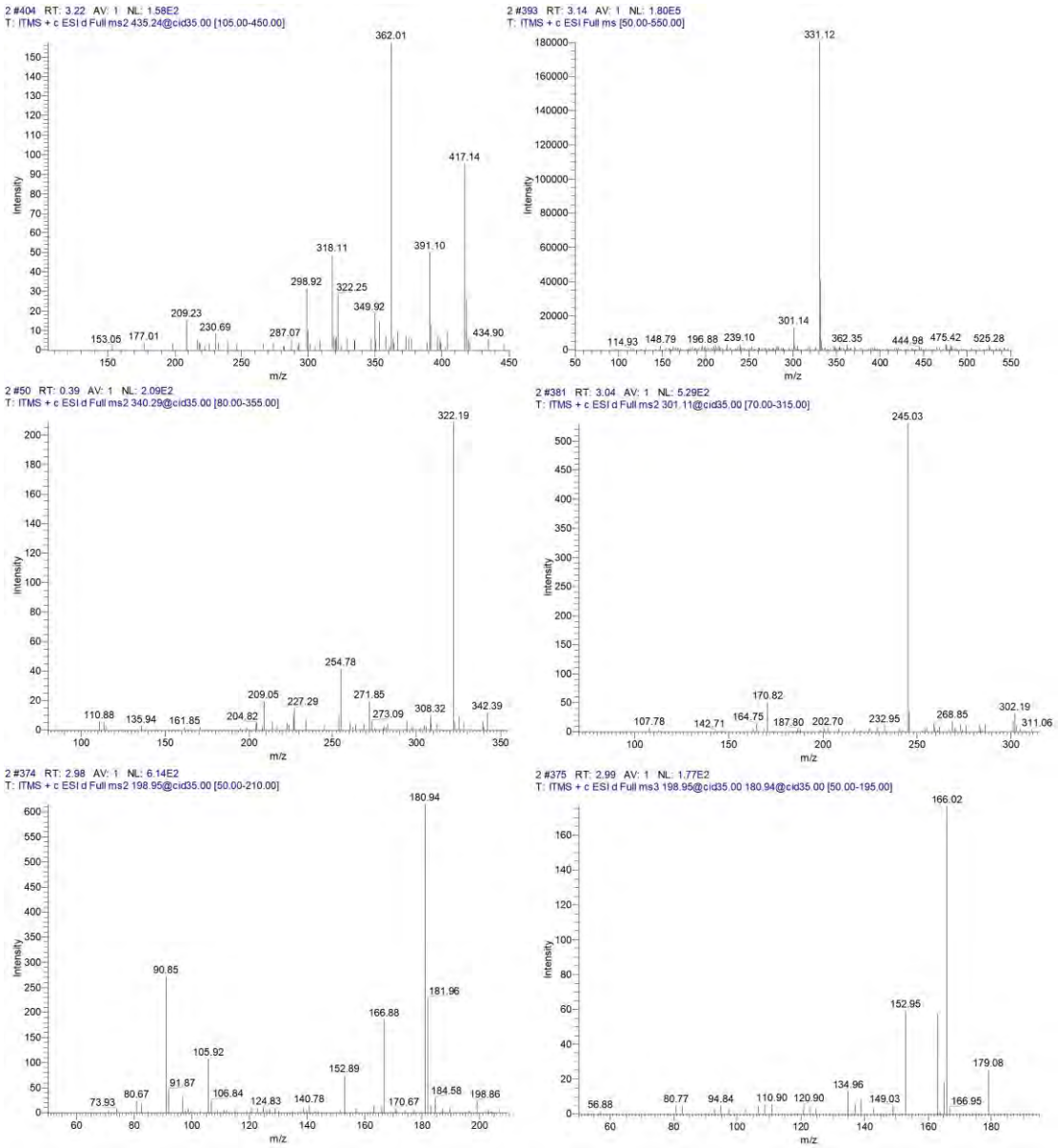

Fig. S3 LC-MS spectra of RhB and its intermediates that appeared in the photodegradation process.

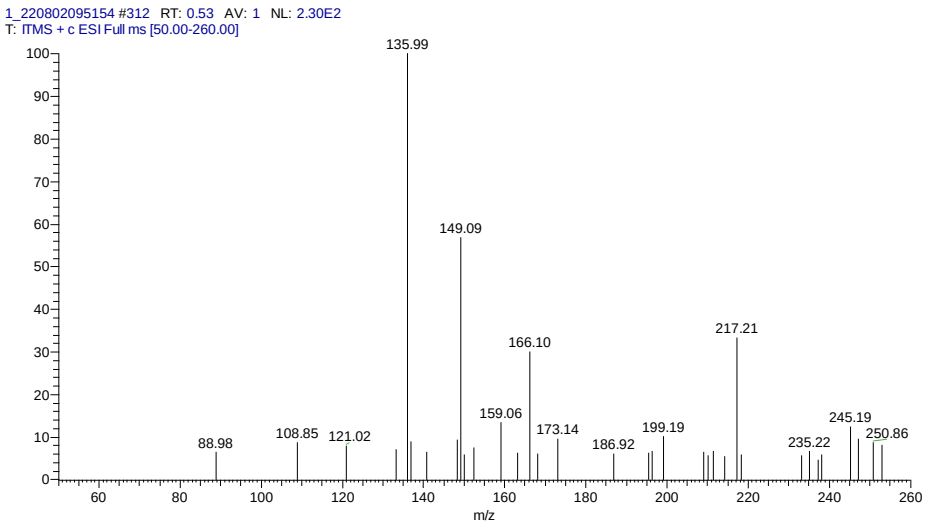

Fig. S4 The corresponding MS spectra of MBT and its intermediates.

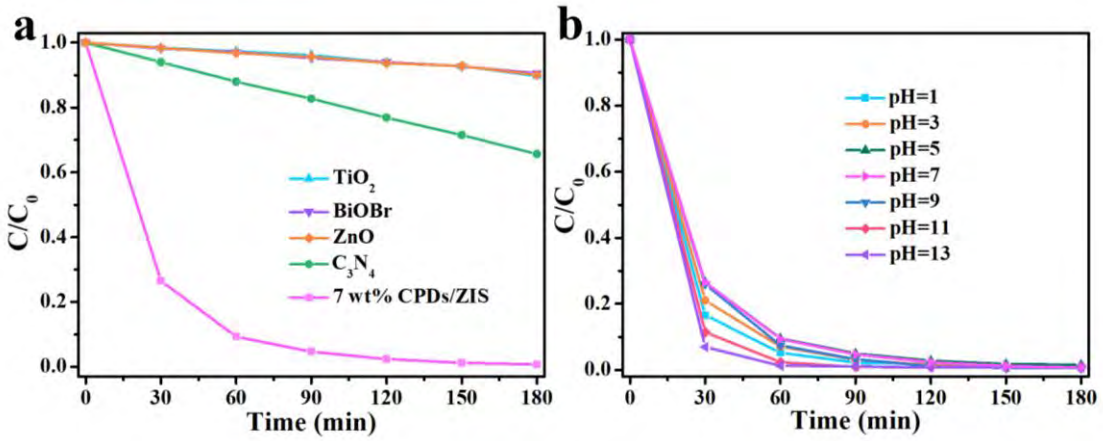

Fig. S5 (a) Photocatalytic properties of different photocatalysts for degradation of RhB under visible light irradiation, (b) Effects of different pH values on the degradation of RhB.

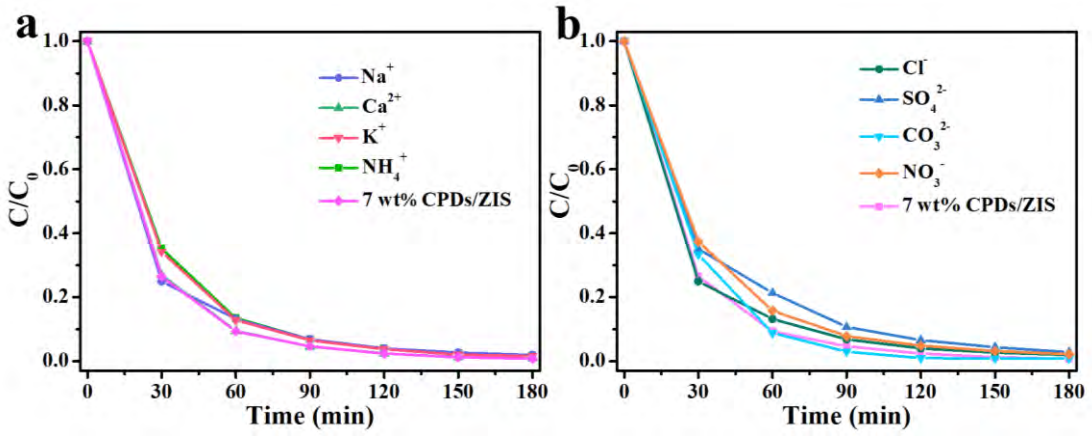

Fig. S6 Effects of (a) cations and (b) anions on the degradation of RhB.

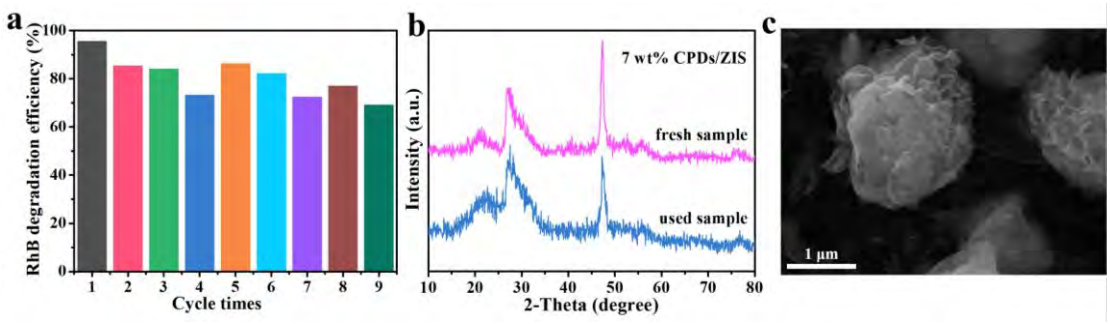

Fig. S7 (a) cycling experiments, (b) XRD patterns and (c) SEM of 7 wt% CPDs/ZIS after circulation.